In situ synthesis of N-containing CoCrFeNi high entropy alloys with enhanced properties fabricated by selective laser melting

Yongyun Zhang [a,c], Shulong Ye [d], Haibo Ke [c,*], K.C. Chan [b,*], Weihua Wang [c,e]

[a] Research Institute for Advanced Manufacturing, Department of Industrial and Systems Engineering, The Hong Kong Polytechnic Univeristy, Hong Kong, China
[b] State Key Laboratory of Ultra-precision Machining Technology, Department of Industrial and Systems Engineering, The Hong Kong Polytechnic University, Hong Kong, China
[c] Songshan Lake Materials Laboratory, Dongguan 523808, China
[d] Faculty of Materials Science, Shenzhen MSU-BIT University, Shenzhen 518172, China
[e] Institute of Physics, Chinese Academy of Sciences, Beijing 100190, China

HIGHLIGHTS

- Quantificationally design of N contents in CoCrFeNi HEA fabricated by SLM.
- N-induced slightly grain refinement without changing heterogeneous microstructure.
- N-induced strength improvement but ductility loss to a varying degree.
- The main contributor to strength improvement was nitrogenous solid solution effect.
- N within a limit would increase SFE then hinder the TWIP effect during deformation.

GRAPHICAL ABSTRACT
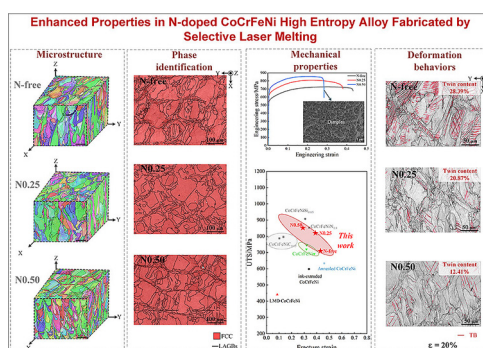
ABSTRACT

Although there have been extensive studies on CoCrFeNi high entropy alloys (HEAs), they are still far from industrial applications due to their inferior strength. Based on the approach of interstitial atom strengthening which has been shown to be one of the effective ways to modify the properties of metallic materials, a series of $(CoCrFeNi)_{100-x}N_x$ (x = 0, 0.25 and 0.50 at. %) HEAs were prepared in this study by selective laser melting (SLM). It was found that nitrogen addition in CoCrFeNi HEA can slightly refine the microstructure but did not change the preferred orientations after SLM. By increasing the nitrogen content in the matrix, the strength increases while the ductility is reduced. Also, the addition of nitrogen in CoCrFeNi HEA can decrease the stacking fault probability, leading to the increased stacking fault energy (SFE) in N-doped CoCrFeNi HEA. The increased strength in N-doped CoCrFeNi HEA samples mainly attributes to the solid solution strengthening of nitrogen, whereas the ductility loss results from the impediment on the formation of deformed twins induced by increased SFE. These results can provide a new strategy for designing high-strength N-doped HEAs.

1. Introduction

In designing traditional alloys, a basic strategy is to add small amounts of secondary elements into the principal element matrix, such as well-used steels, aluminium alloys and copper alloys [1]. A new concept for alloy design was proposed by Yeh et al. [2] and

* Corresponding authors.
  E-mail addresses: kehaibo@sslab.org.cn (H. Ke), kc.chan@polyu.hk (K.C. Chan).

Cantor et al. [3] in mixing five or more main elements with fractions ranging from 5 to 35 at. %. Due to the high configurational entropy by mixing multiple elements to suppress compound formation, these alloys with multiple elements are categorized as high entropy alloys (HEAs), and have totally broadened the design strategy for alloys. Owing to their unique properties, such as an excellent combination of high strength and ductility [4], good oxidation resistance [5], and exceptional high temperature microstructural and mechanical properties [6], HEAs have great potential for applications ranging from aerospace to automobiles [7]. As one of the well-studied HEAs, equimolar CoCrFeNi HEA has a face-centred cubic (FCC) structure and superior toughness, especially at cryogenic temperatures [8]. However, CoCrFeNi HEA is generally considered as the matrix in multiphase HEAs when introducing alloy elements [9–12] due to the poor strength, far from adequate for industrial applications [13].

In an equimolar CoCrFeNi HEA, the relatively low stacking fault energy (SFE) of 32.5 mJ/m^2 [14] triggers the twinning-induced plasticity (TWIP) phenomenon resulting in superior plasticity and strength [15]. Several different approaches have focused on improving the mechanical properties of CoCrFeNi HEA, including grain boundary strengthening [16,17], precipitation strengthening [10,11,18–20], the formation of nanotwins by pre-straining [17,21] and interstitial solute atoms strengthening. It is well known that the formation of the interstitial solid solution has been widely applied in designing traditional alloys, such as steels [22–24] and Ti-based alloys [25] with improved properties. C, B, N, O and Si are the most commonly used interstitial atoms owing to the huge atom radius difference, which enable them to dissolve into the lattice intervals and cause huge lattice distortion. These interstitial atoms have also been shown to significantly improve the properties of HEAs. Carbon is one of the most studied elements that can be used in steels [26], nickel alloys [27] and HEAs [28–30]. For example, adding 3.3 at. % carbon to the $Fe_{40}Mn_{40}Co_{10}Cr_{10}$ HEA matrix can achieve the goal of improving the ductility and strength synchronously [31]. Boron has also been used for enhancing property of HEAs, apart from its common uses in the intermetallics area [32], like the addition of boron to increase the strength of FeCoNiCrMn HEA due to the enhanced grain boundary (GB) cohesion [33]. Oxygen, with a large solid solubility in HEAs composed with Ti, Zr, Hf, V, Nb, Ta elements [34], has been proven to provide effective interstitial atoms for mechanical properties optimization in equimolar HfNbTiZr refractory HEAs [35]. Among the interstitial elements, nitrogen has the widest application in austenitic steels [22–24,36,37] which can provide stable FCC phases [23] and improve strength without worsening ductility significantly in CoCrFeNiMn HEA. However, more work is required to fully understand the strengthening mechanism induced by the interstitial atoms.

The common strategies for HEAs fabrication are arc melting [2], induction melting [3], and metallurgy powder methods including mechanical alloying followed by spark plasma sintering [38] as well as pressure-less sintering [39]. All these methods are time-consuming and require complex post-processing processes for producing HEAs, especially with intricate geometries. The additive manufacturing (AM) method, generally a layer-by-layer building process [40], is notably appropriate for designing HEAs with complex structures, having the unique nature of flexibility and design freedom, as well as higher heating/cooling rates [41] which can hinder the formation of harmful intermetallic compounds during the fabrication process. Brif *et al.* [42] were the first to attempt to fabricate CoCrFeNi HEA specimens with mechanical properties superior to various engineering materials, such as 316 stainless steel, by the additive manufacturing approach. Later, some other

approaches such as heat-treatment [43,44] and the design of laminated structures [12,45] proved to be effective in improving the mechanical properties. In order to solve the above problem, carbon [46–48], boron [49,50] and silicon [51] have been used as interstitial atoms in laser melting fabrication methods for addressing the issue of poor strength in CoCrFeNi alloys. Nevertheless, the precipitates formed resulted in a worsening fracture strain, no higher than 25 %, in those samples fabricated by the SLM approach [46–48,51]. Recently, with a 1.8 at.% N-doping CoCrFeNi HEA without precipitation was successfully fabricated by SLM to enhance the plasticity and strength synchronously by forming the heterostructures [52]. Moreover, it was reported that the formation of ordered nitrogen complexes in the N -doped CoCrFeMnNi can overcome the strength-ductility trade-off [53]. However, a reduction of ductility was found in N-doped counterparts as fabricated via casting [54–56], requiring more effort to understand the effect of nitrogen on the strength-ductility trade-off.

In our study, the CoCrFeNi samples with different nitrogen content were fabricated via SLM to determine the nitrogenous strengthening effect in the studied HEA system. Labile nitride was added to quantitatively control the nitrogen contents in the as-SLMed specimens, rather than by changing the work atmosphere with N_2 during SLM used in the previous studies [52,53]. The microstructure of the original sample via SLM and after deformation was systematically investigated. The underlying mechanism of the interstitial nitrogen atoms on the mechanical properties of CoCrFeNi alloy was revealed, and the strengthening mechanism of N-doping on CoCrFeNi alloy was explained.

2. Materials and methods

2.1. In situ synthesis of N-doped CoCrFeNi alloys by SLM

Fig. 1 (a) shows the selective laser melting (SLM, SLM 125 HL, Germany) process to fabricate the HEA specimens using the nominal equimolar CoCrFeNi powder, in which 304 stainless steel plates with a dimension of 125 × 125 × 20 mm were used as the substrate. The CoCrFeNi equimolar powders, given in Fig. 1 (b) with nominal sizes between 15 μm and 53 μm, were produced by gas atomization (VMP Inc., China) as the raw materials for the SLM fabrication. For fabricating the N-doped CoCrFeNi HEAs, CrN irregular particles with sizes ranging from 15 μm to 53 μm (Guangzhou METALL group, China) were mixed with the HEA powders in a three-dimensional mixer (Turbula T2F, WAB Group, Switzerland), and the energy disperse spectroscopy (EDS, X-Max, Oxford Instruments, UK) for element mapping is given in Fig. 1 (f). By changing the contents of CrN particles in mixed powder blends, three kinds of powders with different N content of 0 (N-free), 0.25 at. % (N0.25) and 0.50 at. % (N0.50) were used in this study, as shown in Fig. 1 (c–e). The actual nitrogen contents of the original powder were detected via an O&N analyzer (ON736, LECO, USA), which are 0.07 at. %, 0.37 at. % and 0.62 at. %, respectively. Before the SLM process, the substrate was preheated to 150 ℃, and the working chamber was filled with flowing argon gas to reduce the oxygen content below 100 ppm. During the SLM, a scanning rotation of 67°(in Fig. 1 (b)) between different layers was used to reduce the residual stress [57] and hinder the formation of cracks [58]. The laser power and scanning speeds were 225 W and 600 mm/s, with a scanning interval of 100 μm and a layer thickness of 50 μm.

2.2. Properties and structural characterization

After the SLM process, the required samples were cut from the substrate by the electric wire-cutting method. The densities of the
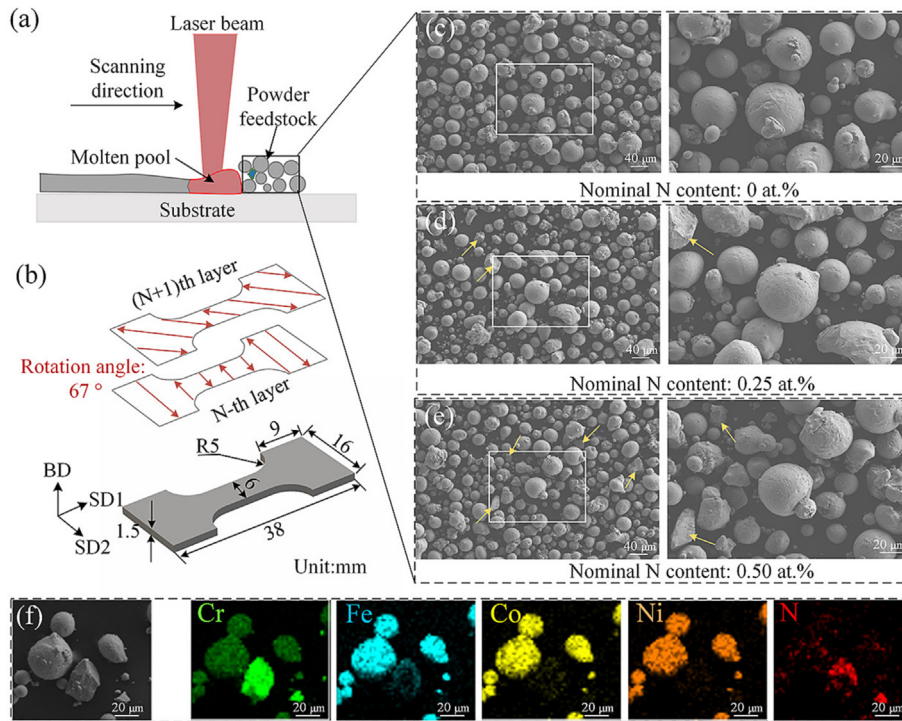
Fig. 1. Fabrication of CoCrFeNi based HEAs specimens: (a) the SLM processing sketch diagram, (b) the tensile bar dimensions with the scanning strategy used in this study, (c–e) powder morphologies with different nominal N contents in SEM, and (f) EDS element maps showing the distribution of CrN particles.

different CoCrFeNi HEAs samples were determined by a densimeter (Sartorius SQP, Germany) based on Archimedes' principle. The nitrogen content was determined by an O&N analyzer (ON736, LECO, USA). The tensile tests were carried out on a tensile testing machine (TestStar Wance, China) by using tensile bars, with dimensions given in Fig. 1 (b), at room temperature with a tensile strain rate of 10^{-3}/s. The surfaces of the tensile bars were ground with abrasive paper and three samples were tested for each testing condition. The fracture surface of the tensile sample was observed in a scanning electron microscope (SEM, Sigma 300, Zeiss, Germany) and the microstructure evolution around the fracture surface was studied using transmission electron microscopy (TEM, JEM F200, Japan) at 200 kV. These samples were ground to 30 μm and then finished by a precision ion polishing system (PIPS II, 695c, USA). The stretched as-SLMed HEAs at the strain levels of 10 %, 20 %, as well as the fractured state, were characterized via the electron backscattered diffraction (EBSD, C-nano, Oxford Instruments, UK) under the step size of 0.2 μm to study the microstructure evolution during the deformation.

In addition, the microstructure on different built surfaces was evaluated using SEM equipped with EBSD (C-nano, Oxford Instruments, UK) under the step size of 2 μm and synchronous collection of EDS. These samples were cut and then ground on abrasive paper finished with 2000 mesh. Then, the ground samples were polished to a scratches-free state and underwent fine-polishing with 50 nm-sized SiO_2 oxide particles solution (OPS, Buehler, USA). The phase composition was examined using X-ray diffraction equipped with a 2D multi-dimensional semiconductor detector (XRD, SmartLab, Japan) with a step size of 0.01°for a range of 2θ ranging from 40 to 100°. The XRD results were post-processed by CMPR software [59] to calculate the dislocation density and the stacking fault probability. The samples from different as-SLMed specimens with differential N contents were also observed in TEM to study the dislocation morphology.

3. Experimental results

3.1. Microstructure of as-SLMed samples

Fig. 2 gives the microstructure and related information obtained by EBSD from as-SLMed samples with different N contents. As the tensile test direction is parallel to XY surface, the grain size distributions on the XY surfaces were analyzed via EBSD results, as shown in Fig. 2 (a_1–a_3). It shows that a smaller grain size was formed by increasing the nitrogen content, exhibiting a similar trend as previous N-doped HEAs [52]. The EBSD orientation maps on the XY planes perpendicular to building direction (BD) for different nominal N content samples are illustrated in Fig. 2 (b_1–b_3), depicting that the coarse columnar grain and fine equiaxed grains are distributed on the XY surface. The three-dimensional EBSD orientation figures from as-SLMed HEA samples with different nominal N content from 0 to 0.50 at. % are displayed in Fig. 2 (c_1–c_3). By increasing the N content in the SLMed samples, the preferred orientation and the crystal morphologies were not significantly changed. From the YZ planes parallel to the BD, the atypical columnar grains, compared to those SLMed samples fabricated with a simple reciprocating scanning strategy [60], were formed based on a cellular growth mode along the BD [60] during the solidification process in SLM. Fig. 2 (d_1–d_3) illustrate the Kernel Average Misorientation (KAM) maps from the YZ planes, which can be used to illustrate that higher misorientations are mainly distributed at grain boundaries regardless of the nitrogen content changes which is similar to the conclusion given by Lin et al [51]. The texture was analyzed by the pole figures and the inverse pole figures shown in Fig. 3 on the XY planes from HEA samples with different nitrogen contents. Strong textures of ⟨110⟩ along BD were developed regardless of the increase of nitrogen content, while the weak texture of ⟨001⟩ along SD was observed by increasing the nitrogen contents.
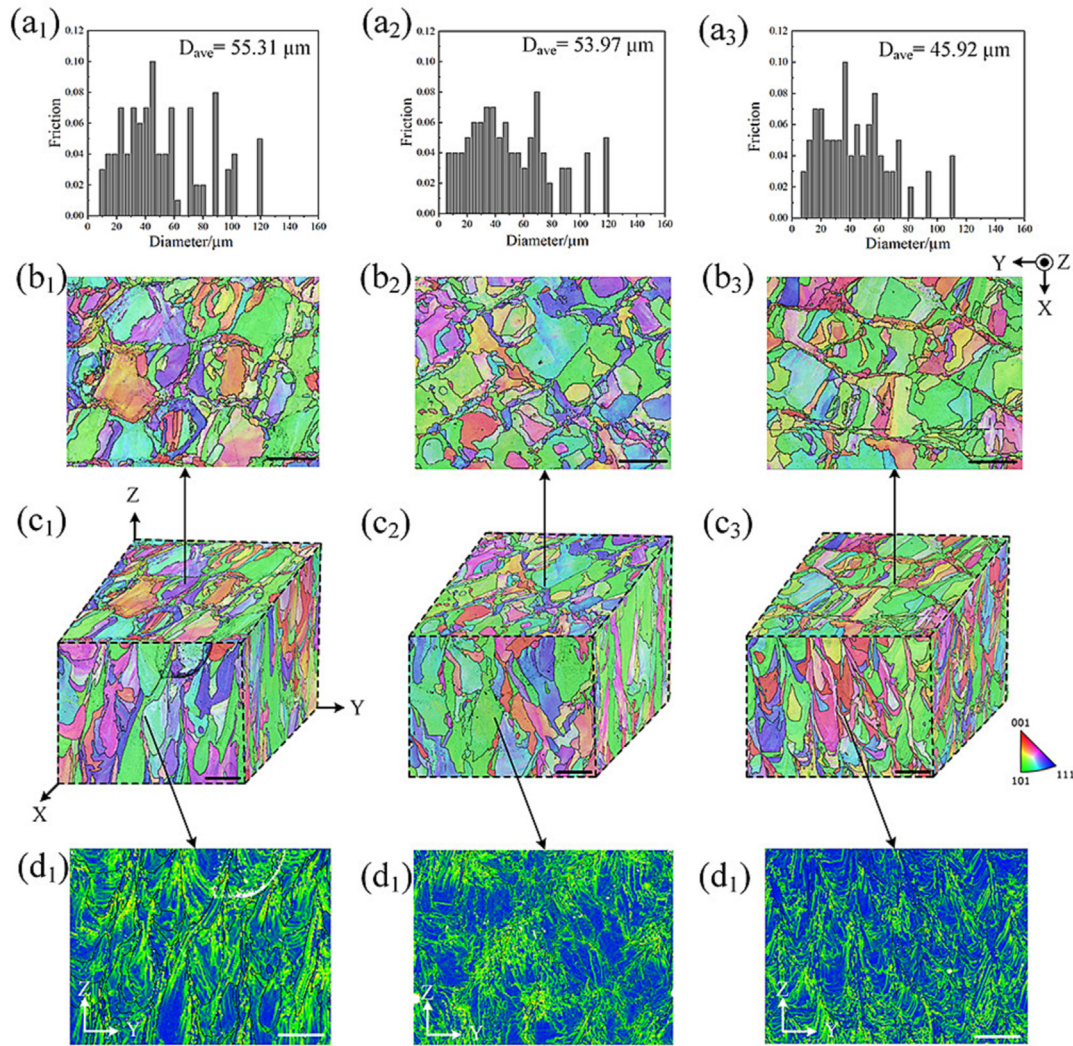
Fig. 2. Grain size charts of (a_1) N-free, (a_2) N0.25 and (a_3) N0.50 samples collected from corresponding EBSD orientations maps on the XY planes (b_1–b_3), which are sampling via the three-dimensional EBSD orientation maps (c_1–c_3); and (d_1-d_3) give the KAM figures of YZ surfaces from the as-SLMed samples with different nominal N contents (scale bar: 100 μm).
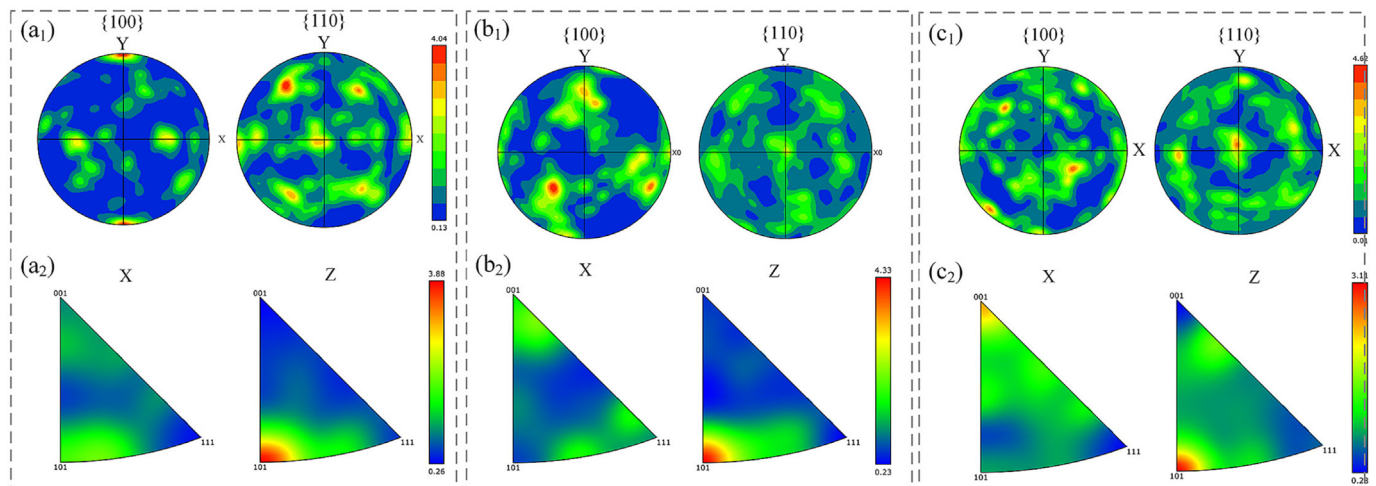

Fig. 3. The pole figues on XY planes from (a_1) N-free, (b_1) N0.25 and (c_1) N0.50 samples and corresponding inverse pole figures (a_2-c_2).
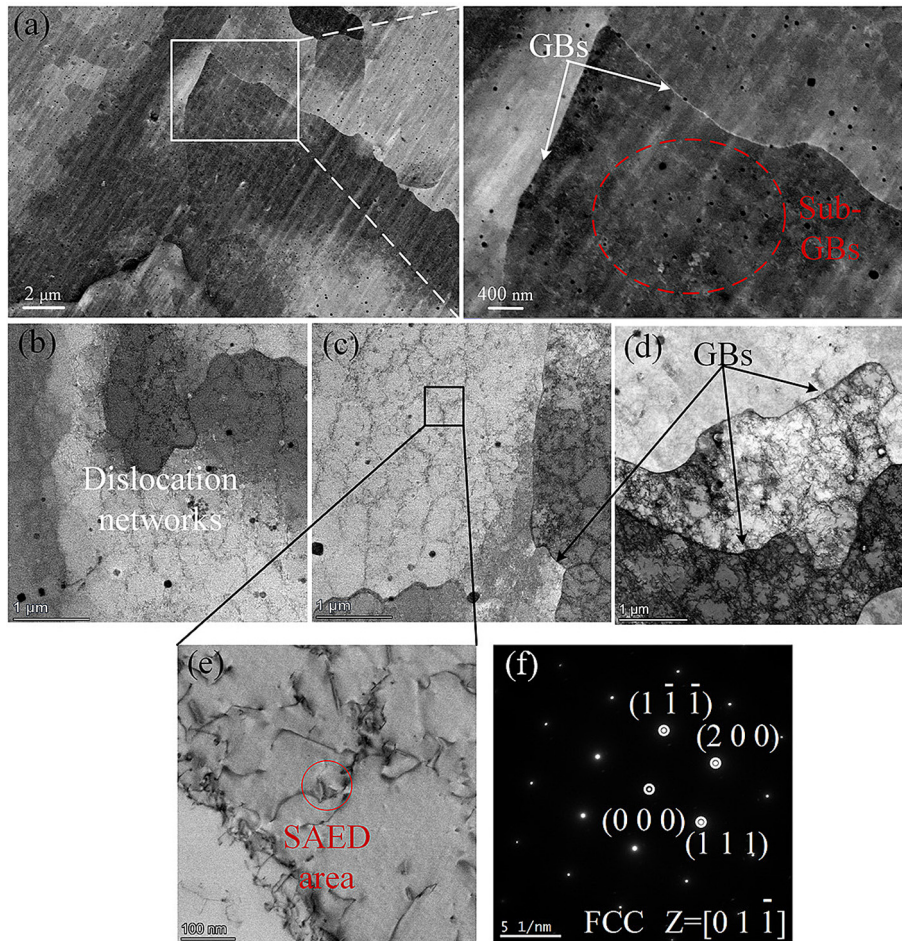
Fig. 4. Submicron microstructure in (a) ECC imaging figures showing the presence of subgrains, (b-e) show the dislocation networks in different samples with increasing N contents, (e) shows the dislocation networks and (f) SAED pattern of FCC structure with the zone axis (Z) of [0 1 −1].

Fig. 4 shows the submicron microstructures of as-SLMed samples in ECC imagining and TEM. In ECC imagining (Fig. 4 (a)), a number of sub-GBs is formed after SLM. These structures were further observed in TEM and proved to be the dislocation networks [43,44,47]. The dislocations in the SLMed samples are formed in the cell structure, of which the boundaries also impede dislocation migration. This is the reason why the SLMed samples' properties are superior as compared to the as-cast specimens [61]. Apart from the cellular structure among all samples, there are some particles observed in the as-SLMed samples, which are generally considered as the oxides in HEAs after SLM [52] under a relative high oxygen level of ~1000 ppm in the SLMed samples detected by an N&O analyzer.

3.2. Phase and elemental composition analysis

The radius of an N atom, 56 pm, is much less than the composed alloying element in the CoCrFeNi HEA matrix. Consequently, the interstitial atoms would be prone to segregate into the lattice intervals and areas near the dislocations. The phase maps acquired from EBSD are given in Fig. 5 (a–c), illustrating that there is a single FCC structure forming after SLM without forming micron-sized nitrides in as-SLMed samples. XRD experiments were performed on different specimens and the XRD profiles are given in Fig. 5 (d). The amplified XRD profiles on the (1 1 1) lattice plane shifts leftwards when nitrogen is introduced into the HEA matrix, indicating that there is an increase of the lattice constant by soluble nitrogen atoms into HEA matrix, and lattice distortion was formed.

It should also be mentioned that there are no nitrides detected by XRD profiles. Fig. 5 (e) gives the TEM figure of N0.25 sample with the corresponding element distribution maps demonstrating a uniform distribution of the elements, regardless of the low hyposensitivity to nitrogen in the EDS system. Hence, the nitrogen contents of different samples were measured by a N&O analyzer and the results show that there is little nitrogen content in the N-free sample of >150 ppm, while the contents in the other two samples are ~780 ppm (~0.31 at. %) and ~1300 ppm (~0.52 at. %). The detected nitrogen contents in those as-SLMed specimens were lower than the actual nitrogen contents in the mixed powder due to the nitride denitrification under the extreme heat cycle during SLM, but the nominal nitrogen content is still of acceptable consistency with the experimental results.

3.3. Mechanical properties and deformation behavior

Fig. 6 demonstrates typical engineering tensile curves of as-SLMed samples with different nominal N contents. From Fig. 6 (a), the yield strength ($\sigma_{0.2}$) and the ultra tensile strength (UTS) increase by adding nitrogen to the HEA matrix. In the N-free sample, the average $\sigma_{0.2}$ and UTS are around 530 MPa and 707 MPa, with a fracture strain of ~43%. By increasing the N content to 0.25 at. %, both $\sigma_{0.2}$ and UTS are increased by ~ 100 MPa, with a slight decrease in fracture strain of less than 5%. When the N content was 0.50 at.%, the highest $\sigma_{0.2}$ and UTS were obtained at 730 MPa and 850 MPa, respectively; while the fracture strain decreased to 29 %. The insert figure in Fig. 6 (a) shows the fracture
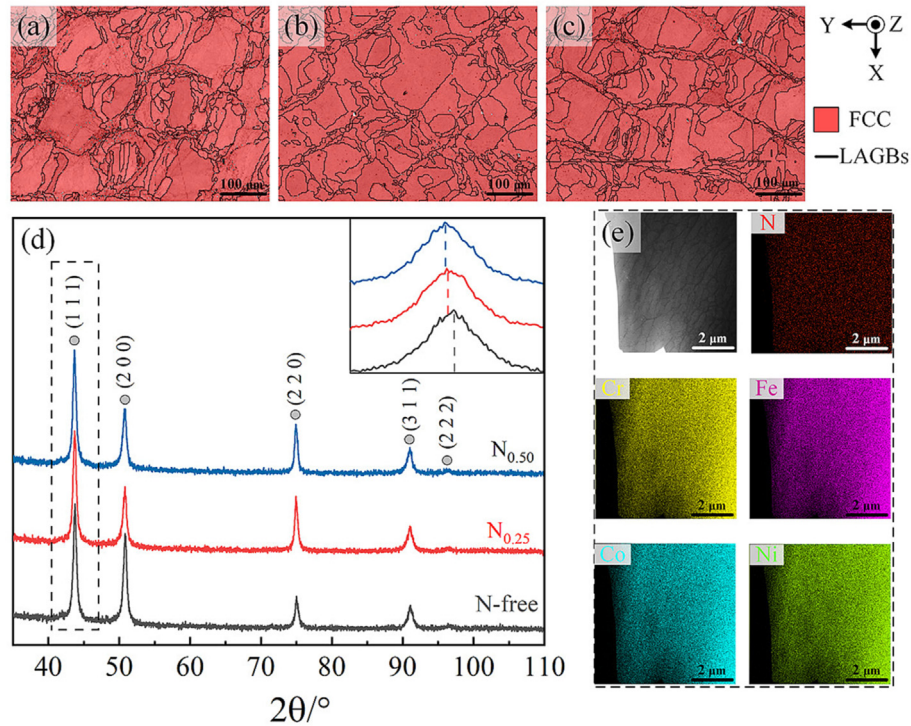
Fig. 5. The phase maps with the high-angle grain boundaries of (a) N-free, (b) N0.25 and (c) N0.50 samples and (d) XRD profiles of as-SLMed samples on the XY planes with insert amplified peak on (1 1 1) plane profile, showing the single phase formed after SLM; and (e) TEM figure from N0.25 sample showing the even element distribution after SLM.
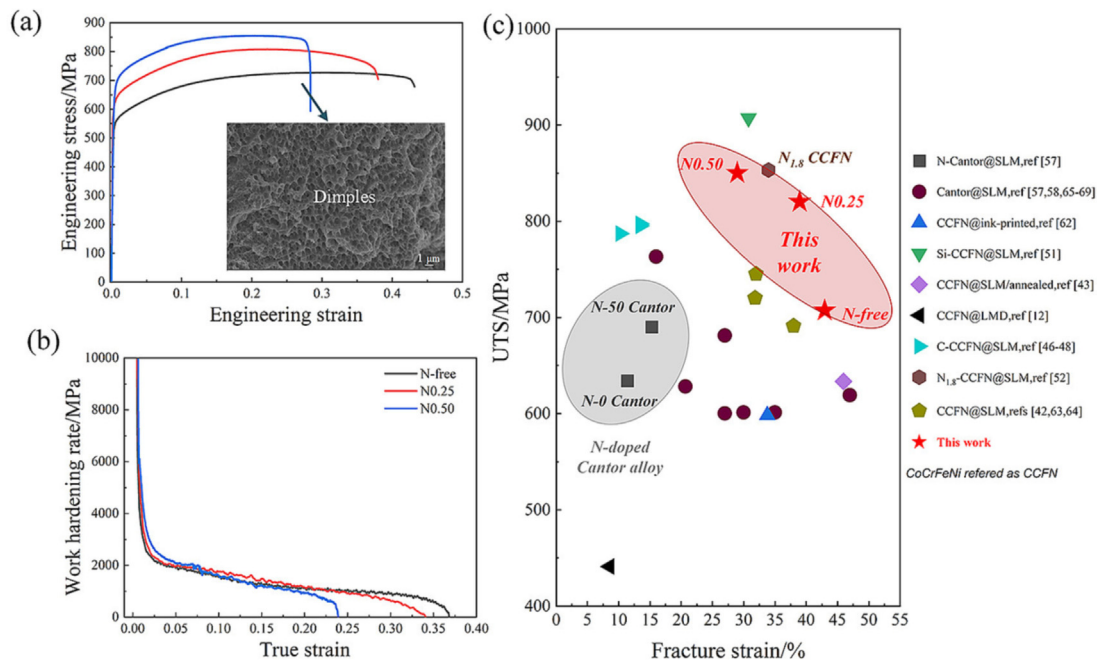

Fig. 6. (a) the typical engineering tensile curves with the fracture surface insert, (b) the corresponding true strain vs working hardening rate curves and (c) the comparison of mechanical properties among CoCrFeNi as well as Cantor HEAs fabricated via additive manufacturing technology.

morphology of the N0.50 sample, exhibiting the typical ductile fracture characteristic of dimples. Fig. 6 (b) compares the work hardening rate in three different N nominal samples. At the beginning stage of plastic deformation, the N-doped HEAs exhibit a higher work hardening rate. Fig. 6 (c) summarizes the strength vs elongation properties of CoCrFeNi as well as CoCrFeNiMn HEAs fabricated by additive manufacturing methods. Fig. 6 (c) compares the mechanical properties of CoCrFeNibased HEAs fabricated by the additive manufacturing approaches, including the ink-extrusion [62], laser melting deposition (LMD) [12] and SLM [42,63,64]. Compared to the other AM approaches, SLM can be used for the fabrication of CoCrFeNi HEA specimens with superior

mechanical properties. The annealing method is an effective way to improve the ductility of SLMed samples [43], while the interstitial atom strengthening, like Si [51], C [46–48] and N [52], would improve the strength of SLMed samples and weaken the ductility in general. In this study, the N-free samples exhibited superior ductility compared to those samples fabricated by SLM [42,63,64], LMD [12] and ink-extrusion [62]. By adding N with an atomic fraction of 0.25 %, the strength was improved without much reduction of the ductility. Although the strength of N0.25 sample was slightly inferior to the N-doped CoCrFeNi HEA with a N content of 1.8 at. % (CoCrFeNiN$_{1.8}$) [52], a better ductility was obtained as compared to the CoCrFeNiN$_{1.8}$ HEA in the previous study [52]. The N-doped CoCrFeNiMn (Cantor) alloys fabricated via SLM were also reported to show the overcoming effect of the strength-ductility trade-off [53] (Gray ellipse in Fig. 6 (c)), while the strength-ductility synergy of N-doped Cantor alloys is worse than that in as-SLMed Cantor alloy counterparts [57,58,65–69]. The CoCrFeNi alloys show better-performed mechanical properties than those Cantor alloys as shown in Fig. 6 (c). In particular, the N-doped CoCrFeNi alloy (this work) has a competitive strength-ductility combination as compared to N-doped Cantor alloys previously reported [53].

As the strength-ductility trade-off occurs in those N-doped CoCrFeNi HEAs in this study after SLM, showing a different trend as compared to their CoCrFeNiN$_{1.8}$ HEA counterpart [52]. The microstructure evolution during the deformation was studied via EBSD on the XY surfaces from as-SLMed HEAs with different nitrogen contents. The overlayed band contrast (BC) and twin boundary figures were collected on those specimens under different strain levels, displayed in Fig. 7 (a). When the pre-stretching strain is

20 %, the N-free sample has the largest amount of deformed twins (21.89%), while the N0.50 sample has the lowest amount of deformed twins (12.41%), showing a similar trend in those samples with a strain level of 10%. It should be mentioned that the N-free sample, with the highest fracture strain, still has the most content of deformed twins around the fracture areas compared to those N-doped specimens. Some typical deformed areas on the fracture surfaces of different samples were also examined by TEM. Fig. 7 (b–d) demonstrate the formation of deformation twins in different samples, supporting the EBSD results shown in Fig. 7 (a). By increasing the N content in the CoCrFeNi matrix, the N-doped HEAs show a reduced ductility, due to a decreased twins content. On the other hand, the addition of nitrogen also affects the formation mechanism of the deformation twins, which is discussed in the following section.

4. Discussion

4.1. Influence of N on the stacking fault probability

The stacking fault energy is the energy consumed during the transformation of perfect dislocations into partial dislocations [70], and determines the critical resolved shear stress (CRSS) for twinning formation. In general, shorter slipping bands would be formed in the lower SFE materials, while wider stacking faults would be produced in materials with higher stacking fault probabilities [71]. Technically, the chemical composition determines the SFE in particular HEAs, and the addition of interstitial atoms affects the SFE. The commonly used method for calculating the SFE of materials is the first-principles calculation [37]. Compared
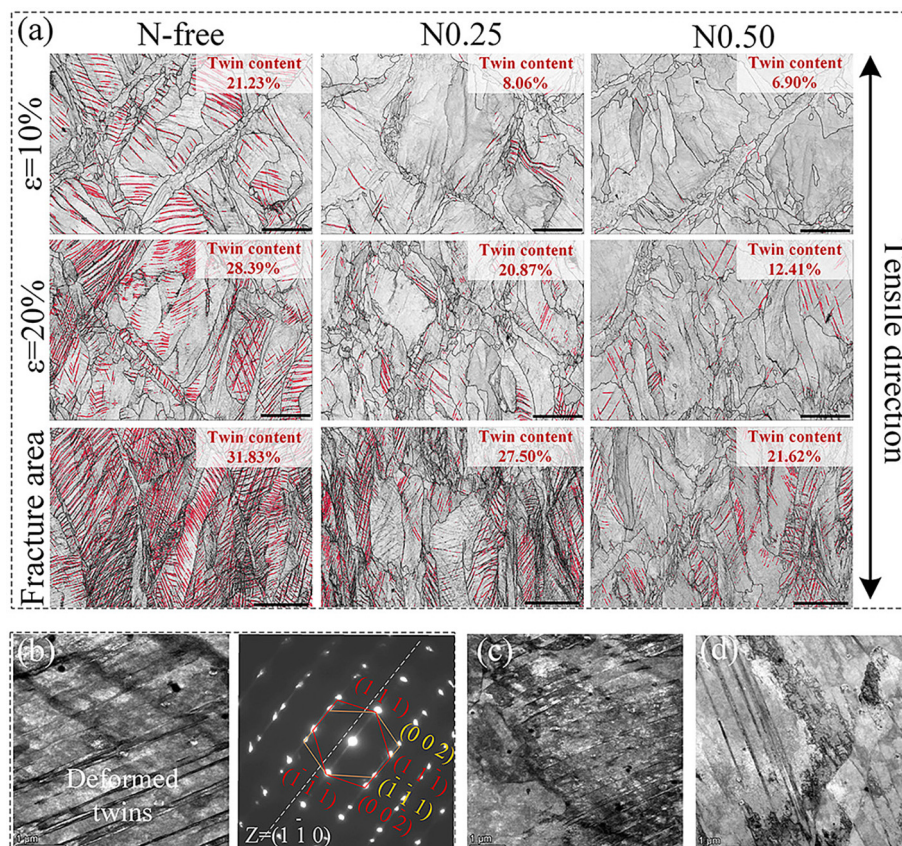

Fig. 7. Deformed microstructure on XY surfaces at different strain levels for each sample of (a) EBSD overlayed BC and twin boundaries figures, showing the twins content difference (scale bar: 50 μm), and TEM figures near fracture surfaces at different local strains of (b) N-free sample with the corresponding SAED pattern, (c) N 0.25 and (d) N0.50 samples.

with this time-consuming method, the XRD method can be used for the calculation of stacking fault probability, which is used for qualitatively studying the SFE changing trend by adding N into the HEA matrix.

The existence of stacking faults induces a slight peak shift. For increasing the precision of the calculated SFE, a pair of reversely shifted XRD peaks, generally (1 1 1) and (2 0 0) peaks, are considered. The peak shift magnitudes are given as follows [72]:

$$\Delta 2\theta_{111} = \frac{90\sqrt{3}\alpha \cdot tan\theta_{111}}{\pi^2}\left(+\frac{1}{4}\right) = 2\theta_{111} - 2\theta_{111}^0 \tag{1}$$

$$\Delta 2\theta_{200} = \frac{90\sqrt{3}\alpha \cdot tan\theta_{200}}{\pi^2}\left(-\frac{1}{2}\right) = 2\theta_{200} - 2\theta_{200}^0 \tag{2}$$

where α is the stacking fault probability, and ±means higher and lower magnitudes compared to those samples without stacking faults. Hence, by differencing Eqs. (1) and (2), Eq. (3) can be obtained:

$$\Delta(\Delta 2\theta_{200} - \Delta 2\theta_{111}) = \frac{-90\sqrt{3}\alpha}{\pi^2}\left(\frac{tan\theta_{200}}{2} + \frac{tan\theta_{111}}{4}\right) \tag{3}$$

In the above equations, stacking fault free samples are required in order to calculate the peak shift magnitudes. However, it is difficult to get stacking fault free samples, especially for alloys with relatively low stacking fault energy. Generally, the relationship between the lattice constant (a^0) and interplanar distance (d^0) is given as:

$$a^0 = \sqrt{3}d_{111}^0 = 2d_{200}^0 \tag{4}$$

And the ratio (constant C) between $\Delta 2\theta_{200}$ and $\Delta 2\theta_{111}$ is given by the following equation:

$$C = \Delta 2\theta_{200}/\Delta 2\theta_{111} = -2\ tan\theta_{200}/\ tan\theta_{111} \tag{5}$$

By Eqs (1), (2) and (5) and Bragg equation, the equation can be acquired in below:

$$2\theta_{200}^0 - C \cdot 2\theta_{111}^0 = 2\theta_{200} - C \cdot 2\theta_{111} = 2arcsin\left(\frac{\lambda}{a}\right) - C \cdot 2arcsin\left(\frac{\sqrt{3}\lambda}{2a}\right) \tag{6}$$

where λ represents the wavelength, 1.5406 Å, of Cu in XRD. By solving the above equations, the stacking fault probability can be determined and is shown in Table 1.

Table 1 shows a decreasing trend in stacking fault probability produced on HEA samples by increasing the N content. In principle, an adverse relationship between SFE and SFP is produced [71]; namely, the addition of the N element into the CoCrFeNi HEA matrix increases the stacking fault energy. This trend is in good agreement with the experimental results on the SFP vs N content in N-doped stainless steels when the N concentration was lower than 0.25 wt% as compared with the N-free sample [22,36]. In addition, the intrinsic SFE increases in N-doped pure Fe were proven by density functional theory results when the N content was 8 at. %[37], which also supports the experimental results in our

study. The SFE (γ_{sf}) can be estimated via the following equation [73]:

$$\gamma_{sf} = 2\rho\Delta G^{\gamma\rightarrow\varepsilon} + 2\sigma^{\gamma/\varepsilon} \tag{7}$$

where ρ is the molar density on the {1 1 1} surface, $\Delta G^{\gamma\rightarrow\varepsilon}$ and $\sigma^{\gamma/\varepsilon}$ represent the Gibbs free energy difference and cohesive energy between the FCC and HCP structure, respectively. Traditionally, N is considered a kind of alloying element, which results in a stable FCC structure in high nitrogen steels [23]. As a result, the dissolved N into the matrix would decrease the Gibbs free energy of the FCC structure; namely, the Gibbs free energy difference ($\Delta G^{\gamma\rightarrow\varepsilon}$) would be expanded, leading to the increase in the SFE on N doped CoCrFeNi HEA specimens.

4.2. Strengthening mechanism in N-doped HEA

The addition of N to the HEA significantly affects the mechanical properties of the SLMed samples. The yield strength is mainly controlled by the dislocation behavior rather than the twinning effect due to the preferential activation of the dislocations compared to twinning [74].To understand the contribution of the strengthening mechanism in N-doped CoCrFeNi HEAs, the contribution of the grain boundaries, solid solution and dislocation to yield strength is given as follows [20]:

$$\sigma_y = \sigma_0 + \Delta\sigma_G + \Delta\sigma_S + \Delta\sigma_D \tag{8}$$

where σ_0 is lattice friction resistance of 165 MPa in CoCrFeNi HEA [20] and the grain boundaries strengthening can be expressed as [75]:

$$\Delta\sigma_G = K_{HP} \cdot d^{-0.5} \tag{9}$$

where K_{HP} is the Hall-Petch coefficient of ~866 MPa·μm$^{-0.5}$ in CoCrFeNi HEA [75,76] and d denotes the grain diameter. However, when N was added to the HEA matrix, the change of K_{HP} due to the alloying element can be estimated via Vegard's law [77]:

$$K_{HP} = \sum_i X_i K_{yi} \tag{10}$$

In this equation, X_i and K_{yi} are the i$_{th}$ element friction (wt. %) and alloying element induced coefficients on K_{HP}, respectively. Norström [24] studied the effect of the N content on the yield strength in 316L stainless steel and based on Eq. (10), the grain-size strengthening coefficient contributed by the nitrogen was estimated to be ~500 MPa·μm$^{-0.5}$. Then, the grain-size strengthening coefficients in N doped HEAs were found to be 886.3 MPa·μm$^{-0.5}$ (N0.25) and 886.6 MPa·μm$^{-0.5}$ (N0.50), respectively. By using the average grain diameter calculated in EBSD on the XY surface, the grain boundary strengths in these three kinds of alloys were 116.4 MPa (N-free), 117.9 MPa (N0.25) and 127.8 MPa (N0.50), respectively.

In HEAs, solution strengthening is generally not considered as there are no principal elements in the HEA matrix [78]. However, the solution strengthening effect should also be present in N doped

Table 1
The parameters used in the stacking fault probability calculation by XRD.

Sample	hkl	2θ /°	a^0 /10^{-10}m	$2\theta^0$ /°	$\triangle(\triangle\theta_{200}-\triangle\theta_{111})$ /°	α /10^{-3}m
CoCrFeNi	111	43.747	3.584	43.710	−0.138	0.4513
	200	50.814		50.915		
(CoCrFeNi)$_{99.75}$N$_{0.25}$	111	43.690	3.588	43.660	−0.084	0.2749
	200	50.800		50.854		
(CoCrFeNi)$_{99.50}$N$_{0.50}$	111	43.669	3.589	43.647	−0.062	0.2030
	200	50.799		50.839		

HEAs. Roth et al. [79] investigated the solution strengthening in Nickel alloys, given by:

$$\Delta\sigma_S = (\sum_i k_i^{1/n} c_i)^n \tag{11}$$

where k_i is the strengthening coefficient factor of element i and c_i is the atomic fraction of solute atoms. When n = 2/3, Eq. (11) can well express the solution strengthening effect of solute atoms. The experimental results of the N-doped CoCrFeNiMn HEA [54] were used for the calculation of the strengthening coefficient factor of element N (k_{iN}), a value of 4765.85 MPa (at.%)$^{-n}$. Hence, the solution strength changes in N-doped CoCrFeNi HEAs are 84.0 MPa (N0.25) and 132.6 MPa (N0.50), respectively.

Another factor that can greatly affect the yield strength is the dislocation density, estimated by Taylor's hardening law [80]:

$$\Delta\sigma_D = M\alpha Gb\rho^{0.5} \tag{12}$$

In the above equation, M and α are Taylor factor of 3.06 [81] and correction constant of 0.2 [82], G represents the shear modulus of 84.3 GPa in the equimolar CoCrFeNi alloy [82], b is the Burgers vector of a $\langle 1\,1\,0\rangle/2$ of 0.234 nm and ρ is the dislocation density. However, the shear modulus would be influenced by the element composition, and can be calculated via the following equation [77]:

$$G = \sum_i c_i G_{ii}^{(0)} \tag{13}$$

where $G_{ii}^{(0)}$ is the shear modulus of the simple substance. In the N-doped HEAs, interstitial N atoms are prone to concentrate in octahedral interstices [83]. Based on the results obtained via density functional theory on N-doped Cantor alloy, the conventional cell with the 20 at. % N was used in that study [83]. Using the calculated results and Eq. (13), the shear modulus contributed by nitrogen can be estimated to be around −550 GPa·(at. %)$^{-1}$, which means that the solute atoms of N would decrease the shear modulus of the N-doped samples. As a result, the shear moduli of N doped HEAs are 82.9 GPa (N0.25) and 81.6 GPa (N0.50), respectively. The required factor of dislocation density can be acquired via Eq. (14) [84]:

$$\rho = \frac{16.1\varepsilon^2}{b^2} \tag{14}$$

where ε is the micro-strain which can be fitted by XRD profiles, based on the following equations [85]:

$$\beta cos\theta = \frac{K\lambda}{D} + 4\varepsilon sin\theta \tag{15}$$

where β represents the fitted full width at half maximum (FWHM) values of different peaks on the XRD profiles, and K is a dimensionless constant of 0.89 [78]. The required XRD peak information of different HEA samples was collected by the CMPR package [59], and the fitted micro strains were obtained. Finally, the dislocation density in different samples were estimated to be $3.493 \times 10^{14} m^{-2}$ in the N-free sample, $3.889 \times 10^{14}\ m^{-2}$ in N$_{0.25}$ sample and $5.996 \times 10^{14}\ m^{-2}$ in N$_{0.50}$ sample, which are at similar density levels as given in the study of Lin et al [51]. A higher solidification shrinkage strain would be produced after the SLM process, which can proceed with the formation of dislocations. When interstitial N atoms are added to the HEA matrix, a stronger hysteresis diffusion effect would hinder the vacancies in being filled, resulting in the formation of more dislocation loops [51], and then increasing the dislocation density by introducing N. As a result, the dislocation density induced yield strength increases are 225.2 MPa (N-free), 233.9 MPa (N0.25) and 285.8 MPa (N0.50), respectively.

Based on the discussion above, the contribution of different aspects to the yield strength of as-SLMed samples with different N contents is presented in Fig. 8 and the detailed calculated results
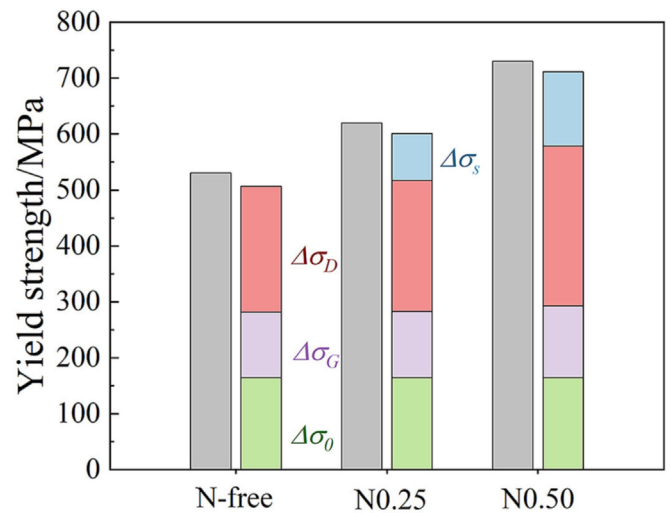

Fig. 8. The experimental yield strength and the calculated strength difference contributed from different aspects.

were also listed in Table 2. The calculated results agreed well with the experimental results. The dislocation strengthening was the main factor contributing to the yield strength of the as-SLMed samples. However, when N was introduced into the HEA system, the interstitial atomic solid solution strengthening would also play an important role in the improvement of the yield strength of interstitial atom doped alloys.

4.3. Effects of N on the mechanical properties of HEA samples

The addition of N into the CoCrFeNi matrix would increase the yield strength of as-SLMed samples. Apart from this, the doping of N would also affect the plastic deformation of as-SLMed samples. N-Free CoCrFeNi HEA has balanced mechanical properties, i.e. superior ductility and acceptable UTS. This is because of a relatively lower SFE of 32.5 mJ/mm^2 in CoCrFeNi [14] and the deformed twins being easily activated during the plastic deformation shown in Fig. 7, especially the SFE is in the range from 15 mJ/mm^2 to 50 mJ/mm^2 [15]. These nano-sized twins would be nucleated on the stacking faults, promoting the formation of twins during deformation. With a kind of material with low/medium SFE, the thickness of the stacking fault would increase and worsen the cross-slip of the dislocations. The slipping of dislocations and the deformation twinning are important methods in the deformation mechanism of the CoCrFeNi HEA. Generally, the twinning would dominate the plastic deformation and would be accompanied by the slipping of dislocations [86]. Under these comprehensive influences, a balanced mechanical property can be formed in the as-SLMed CoCrFeNi HEA sample.

By inducing N into the CoCrFeNi matrix, the strength would be increased, while the fracture strain would be reduced, as shown in Fig. 6. With an N content of 0.25 at. % in the HEA matrix, the UTS would be increased by ~100 MPa., while the fracture strain decreases slightly. The pinning effect of N atoms on the dislocations during the plastic deformation is responsible for the improvement of the strength in N-doped HEA. When dislocations move across the interstitial atom segregation area, more energy is consumed to overcome the resistance from the pinning effect by the N atoms. With the addition of N atoms into the HEA matrix, the N atoms can hinder the dislocation movement, resulting in a higher UTS in N doped CoCrFeNi HEAs and work hardening rate in the previous stage of plastic deformation [87]. With a further increase in the N content of the CoCrFeNi HEA to 0.5. at %, the stacking fault probability decreases, namely, the SFE would

Table 2
The calculated contribution of each aspect to the yield strength in N-doped HEA samples.

Sample	σ_0 /Mpa	$\Delta\sigma_G$ /MPa	$\Delta\sigma_D$ /MPa	$\Delta\sigma_s$ /MPa	Total/ MPa
CoCrFeNi	165.0	116.4	225.2	–	506.6
(CoCrFeNi)$_{99.75}$N$_{0.25}$	165.0	117.9	233.9	84.0	600.8
(CoCrFeNi)$_{99.50}$N$_{0.50}$	165.0	127.8	285.8	132.6	711.2

increase by increasing the N content in the matrix. The thickness of the stacking fault in the decomposition of perfect dislocations is lower than the N-free samples, leading to the suppression of deformation twinning [15] as illustrated in Fig. 7 (a). The continuous formation of deformation twins decreases the mean free path of the dislocations, increasing the driving force for slipping, and increasing the work hardening rate [88,89]. However, with the suppression of deformation twinning by inducing N into the matrix, the work hardening rate in the final deformation stage would be lower than that in the N-free one. On the other hand, an impediment effect on the dislocation movement would be formed and a higher resistance force would be required to activate the ductility deformation [90]. The formation of twins during deformation would hinder the dislocation slipping in the high-strain area, resulting in dislocation slip induced plasticity in the lower strain area and prolonging the formation of necking shrinkage [91]. As a result, in the N doped CoCrFeNi HEA, the twinning would be restrained by the increase of SFE and then the fracture strain would then decrease with increasing N content in CoCrFeNi HEAs.

5. Conclusions

In this study, N-doped CoCrFeNi-based HEAs were fabricated by SLM. The microstructure and mechanical properties of as-SLMed samples were evaluated with different nitrogen contents. The main conclusions are summarized as follows:

(1) Heterogeneous microstructures and dislocation networks were formed in all the as-SLMed samples and their grain size decreased with increasing nitrogen content.
(2) When the nitrogen content was 0.25 at. %, both the yield strength and UTS of the HEA increased by ~100 MPa compared to the N-free sample and there was no obvious ductility loss (less than 5 %). When the nitrogen content was increased to 0.50 at. %, the yield strength and UTS increased to 730 MPa and 850 MPa, respectively, while a fracture strain reduction of ~15 % was observed as compared to the N-free sample.
(3) The solid solution strengthening effect attributed by the solute nitrogen atoms was the main factor that caused the improvement in yield strength and UTS. However, an adverse effect on the SFE was caused by the addition of N into the CoCrFeNi matrix, hindering the TWIP mechanism during the deformation, and leading to the plasticity loss on N-doped CoCrFeNi alloys.

Data availability

Data will be made available on request.

Declaration of Competing Interest

The authors declare that they have no known competing financial interests or personal relationships that could have appeared to influence the work reported in this paper.

References

[1] A. Ostovari Moghaddam, N.A. Shaburova, M.N. Samodurova, A. Abdollahzadeh, E.A. Trofimov, Additive manufacturing of high entropy alloys: a practical review, J. Mater. Sci. Technol. 77 (2021) 131–162, https://doi.org/10.1016/j.jmst.2020.11.029.
[2] J.W. Yeh, S.K. Chen, S.J. Lin, J.Y. Gan, T.S. Chin, T.T. Shun, C.H. Tsau, S.Y. Chang, Nanostructured high-entropy alloys with multiple principal elements: Novel alloy design concepts and outcomes, Adv. Eng. Mater. 6 (2004) 299–303, https://doi.org/10.1002/adem.200300567.
[3] B. Cantor, I.T.H. Chang, P. Knight, A.J.B. Vincent, Microstructural development in equiatomic multicomponent alloys, Mater. Sci. Eng. A. 375–377 (2004) 213–218, https://doi.org/10.1016/j.msea.2003.10.257.
[4] Z. Li, K.G. Pradeep, Y. Deng, D. Raabe, C.C. Tasan, Metastable high-entropy dual-phase alloys overcome the strength-ductility trade-off, Nature. 534 (2016) 227–230, https://doi.org/10.1038/nature17981.
[5] B. Gorr, M. Azim, H.J. Christ, T. Mueller, D. Schliephake, M. Heilmaier, Phase equilibria, microstructure, and high temperature oxidation resistance of novel refractory high-entropy alloys, J. Alloys Compd. 624 (2015) 270–278, https://doi.org/10.1016/j.jallcom.2014.11.012.
[6] X. Yang, D. Sun, Y. Zhou, Y. Gao, S. Xi, H. Wu, C. He, A novel, non-equiatomic NiCrWFeTi high-entropy alloy with exceptional phase stability, Mater. Lett. 263 (2020), https://doi.org/10.1016/j.matlet.2019.127202 127202.
[7] Y.F. Ye, Q. Wang, J. Lu, C.T. Liu, Y. Yang, High-entropy alloy: challenges and prospects, Mater. Today. 19 (2016) 349–362, https://doi.org/10.1016/j.mattod.2015.11.026.
[8] B. Gludovatz, A fracture-resistant high-entropy alloy for cryogenic applications, Science (80-.). 345 (2014) 1153–1158. doi:10.1126/science.1254581.
[9] F. He, Z. Wang, Q. Wu, J. Li, J. Wang, C.T. Liu, Phase separation of metastable CoCrFeNi high entropy alloy at intermediate temperatures, Scr. Mater. 126 (2017) 15–19, https://doi.org/10.1016/j.scriptamat.2016.08.008.
[10] W.H. Liu, Z.P. Lu, J.Y. He, J.H. Luan, Z.J. Wang, B. Liu, Y. Liu, M.W. Chen, C.T. Liu, Ductile CoCrFeNiMox high entropy alloys strengthened by hard intermetallic phases, Acta Mater. 116 (2016) 332–342, https://doi.org/10.1016/j.actamat.2016.06.063.
[11] X. Li, Z. Li, Z. Wu, S. Zhao, W. Zhang, H. Bei, Y. Gao, Strengthening in Al-, Mo- or Ti-doped CoCrFeNi high entropy alloys: a parallel comparison, J. Mater. Sci. Technol. 94 (2021) 264–274, https://doi.org/10.1016/j.jmst.2021.02.060.
[12] Y. Cai, L. Zhu, Y. Cui, J. Han, Manufacturing of FeCoCrNi + FeCoCrNiAl laminated high-entropy alloy by laser melting deposition (LMD), Mater. Lett. 289 (2021), https://doi.org/10.1016/j.matlet.2021.129445 129445.
[13] A.J. Zaddach, R.O. Scattergood, C.C. Koch, Tensile properties of low-stacking fault energy high-entropy alloys, Mater. Sci. Eng. A. 636 (2015) 373–378, https://doi.org/10.1016/j.msea.2015.03.109.
[14] Y. Wang, B. Liu, K. Yan, M. Wang, S. Kabra, Y.L. Chiu, D. Dye, P.D. Lee, Y. Liu, B. Cai, Probing deformation mechanisms of a FeCoCrNi high-entropy alloy at 293 and 77 K using in situ neutron diffraction, Acta Mater. 154 (2018) 79–89, https://doi.org/10.1016/j.actamat.2018.05.013.
[15] A. Pineau, C. Matdriaux, Twinning and strain-induced f.c.c-h.c.p transformation on the mechanical properties of Co-Ni-Cr-Mo alloys, Transformation. 26 (1976) 123–132.

[16] P. Sathiyamoorthi, J. Basu, S. Kashyap, K.G. Pradeep, R.S. Kottada, Thermal stability and grain boundary strengthening in ultrafine-grained CoCrFeNi high entropy alloy composite, Mater. Des. 134 (2017) 426–433, https://doi.org/10.1016/j.matdes.2017.08.053.

[17] W. Huo, F. Fang, H. Zhou, Z. Xie, J. Shang, J. Jiang, Remarkable strength of CoCrFeNi high-entropy alloy wires at cryogenic and elevated temperatures, Scr. Mater. 141 (2017) 125–128, https://doi.org/10.1016/j.scriptamat.2017.08.006.

[18] M.A. Haq, Y. Song, M.W. Khalid, D.W. Jeong, K.T. Park, J.G. Kim, M.H. Lee, B.S. Kim, Designing co-reinforced in-situ (Cr3C2(w) + Cr2O3(p))/CoCrFeNi composite with excellent strengthening efficiency, Mater. Sci. Eng. A. 832 (2022), https://doi.org/10.1016/j.msea.2021.142365 142365.

[19] S. Lee, D. Chatain, C.H. Liebscher, G. Dehm, Structure and hardness of in situ synthesized nano-oxide strengthened CoCrFeNi high entropy alloy thin films, Scr. Mater. 203 (2021), https://doi.org/10.1016/j.scriptamat.2021.114044 114044.

[20] J.Y. He, H. Wang, H.L. Huang, X.D. Xu, M.W. Chen, Y. Wu, X.J. Liu, T.G. Nieh, K. An, Z.P. Lu, A precipitation-hardened high-entropy alloy with outstanding tensile properties, Acta Mater. 102 (2016) 187–196, https://doi.org/10.1016/j.actamat.2015.08.076.

[21] Z. Zhang, Z. Jiang, Y. Xie, S.L.I. Chan, J. Liang, J. Wang, Multiple deformation mechanisms induced by pre-twinning in CoCrFeNi high entropy alloy, Scr. Mater. 207 (2022), https://doi.org/10.1016/j.scriptamat.2021.114266 114266.

[22] M. Fujikura, K. Takada, K. Ishida, Effect of manganese and nitrogen on the mechanical properties of Fe-18%Cr-10%Ni steels, Trans. Iron Steel Inst. Jap. 15 (1975) 464–469, https://doi.org/10.2355/isijinternational1966.15.464.

[23] R.P. Reed, Nitrogen in austenitic stainless steels, Jom. 41 (1989) 16–21, https://doi.org/10.1007/BF03220991.

[24] L. Norström, The influence of nitrogen and grain size on yield strength in type AISI 316L austenitic stainless steel, Met. Sci. 11 (1977) 208–212, https://doi.org/10.1179/msc.1977.11.6.208.

[25] Q. Yu, L. Qi, T. Tsuru, R. Traylor, D. Rugg, J.W. Morris, M. Asta, D.C. Chrzan, A.M. Minor, Origin of dramatic oxygen solute strengthening effect in titanium, Science (80-.). 347 (2015) 635–639. doi:10.1126/science.1260485.

[26] V.A. Shabashov, L.G. Mukoseev, A.G. Makarov, V.V. Sagaradze, A.V. Makarov, V.P. Pilyugin, S.I. Novikov, N.F. Vildanova, Deformation-induced phase transitions in a high-carbon steel, Mater. Sci. Eng. A. 346 (2003) 196–207, https://doi.org/10.1016/S0921-5093(02)00549-X.

[27] R.G. Thompson, D.E. Mayo, B. Radhakrishnan, The relationship between carbon content, microstructure, and intergranular liquation cracking in cast nickel alloy 718, Metall. Trans. A. 22 (1991) 557–567, https://doi.org/10.1007/BF02656823.

[28] J.G. Kim, J.M. Park, J.B. Seol, J. Choe, J.H. Yu, S. Yang, H.S. Kim, Nano-scale solute heterogeneities in the ultrastrong selectively laser melted carbon-doped CoCrFeMnNi alloy, Mater. Sci. Eng. A. 773 (2020), https://doi.org/10.1016/j.msea.2019.138726 138726.

[29] L.J. Zhang, P.F. Yu, J.T. Fan, M.D. Zhang, C.Z. Zhang, H.Z. Cui, G. Li, Investigating the micro and nanomechanical properties of CoCrFeNi-Cx high-entropy alloys containing eutectic carbides, Mater. Sci. Eng. A. 796 (2020), https://doi.org/10.1016/j.msea.2020.140065.

[30] K.S. Chung, J.H. Luan, C.H. Shek, Strengthening and deformation mechanism of interstitially N and C doped FeCrCoNi high entropy alloy, J. Alloys Compd. 904 (2022), https://doi.org/10.1016/j.jallcom.2022.164118 164118.

[31] L.B. Chen, R. Wei, K. Tang, J. Zhang, F. Jiang, L. He, J. Sun, Heavy carbon alloyed FCC-structured high entropy alloy with excellent combination of strength and ductility, Mater. Sci. Eng. A. 716 (2018) 150–156, https://doi.org/10.1016/j.msea.2018.01.045.

[32] C.T. Liu, C.L. White, J.A. Horton, Effect of boron on grain-boundaries in Ni3Al†, Acta Metall. 33 (1985) 213–229, https://doi.org/10.1016/0001-6160(85)90139-7.

[33] J.B. Seol, J.W. Bae, Z. Li, J. Chan Han, J.G. Kim, D. Raabe, H.S. Kim, Boron doped ultrastrong and ductile high-entropy alloys, Acta Mater. 151 (2018) 366–376, https://doi.org/10.1016/j.actamat.2018.04.004.

[34] H. Okamoto, H. Okamoto, Phase Diagrams for Binary Alloys, ASM international Materials Park, OH, 2000.

[35] Z. Lei, X. Liu, Y. Wu, H. Wang, S. Jiang, S. Wang, X. Hui, Y. Wu, B. Gault, P. Kontis, D. Raabe, L. Gu, Q. Zhang, H. Chen, H. Wang, J. Liu, K. An, Q. Zeng, T.G. Nieh, Z. Lu, Enhanced strength and ductility in a high-entropy alloy via ordered oxygen complexes, Nature. 563 (2018) 546–550, https://doi.org/10.1038/s41586-018-0685-y.

[36] I.A. Yakubtsov, A. Ariapour, D.D. Perovic, Effect of nitrogen on stacking fault energy of f.c.c. iron-based alloys, Acta Mater. 47 (1999) 1271–1279, https://doi.org/10.1016/S1359-6454(98)00419-4.

[37] S. Kibey, J.B. Liu, M.J. Curtis, D.D. Johnson, H. Sehitoglu, Effect of nitrogen on generalized stacking fault energy and stacking fault widths in high nitrogen steels, Acta Mater. 54 (2006) 2991–3001, https://doi.org/10.1016/j.actamat.2006.02.048.

[38] R.M. Pohan, B. Gwalani, J. Lee, T. Alam, J.Y. Hwang, H.J. Ryu, R. Banerjee, S.H. Hong, Microstructures and mechanical properties of mechanically alloyed and spark plasma sintered Al0.3CoCrFeMnNi high entropy alloy, Mater. Chem. Phys. 210 (2018) 62–70, https://doi.org/10.1016/j.matchemphys.2017.09.013.

[39] N. Eißmann, B. Klöden, T. Weißgärber, B. Kieback, High-entropy alloy CoCrFeMnNi produced by powder metallurgy, Powder Metall. 60 (2017) 184–197, https://doi.org/10.1080/00325899.2017.1318480.

[40] D. Herzog, V. Seyda, E. Wycisk, C. Emmelmann, Additive manufacturing of metals, Acta Mater. 117 (2016) 371–392, https://doi.org/10.1016/j.actamat.2016.07.019.

[41] N. Li, S. Huang, G. Zhang, R. Qin, W. Liu, H. Xiong, G. Shi, J. Blackburn, Progress in additive manufacturing on new materials: a review, J. Mater. Sci. Technol. 35 (2019) 242–269, https://doi.org/10.1016/j.jmst.2018.09.002.

[42] Y. Brif, M. Thomas, I. Todd, The use of high-entropy alloys in additive manufacturing, Scr. Mater. 99 (2015) 93–96, https://doi.org/10.1016/j.scriptamat.2014.11.037.

[43] D. Lin, L. Xu, H. Jing, Y. Han, L. Zhao, F. Minami, Effects of annealing on the structure and mechanical properties of FeCoCrNi high-entropy alloy fabricated via selective laser melting, Add. Manuf. 32 (2020), https://doi.org/10.1016/j.addma.2020.101058 101058.

[44] D. Lin, L. Xu, H. Jing, Y. Han, L. Zhao, Y. Zhang, H. Li, A strong, ductile, high-entropy FeCoCrNi alloy with fine grains fabricated via additive manufacturing and a single cold deformation and annealing cycle, Add. Manuf. 36 (2020), https://doi.org/10.1016/j.addma.2020.101591 101591.

[45] Y. Cai, X. Li, H. Xia, Y. Cui, S.M. Manladan, L. Zhu, M. Shan, D. Sun, T. Wang, X. Lv, J. Han, Fabrication of laminated high entropy alloys using differences in laser melting deposition characteristics of FeCoCrNi and FeCoCrNiAl, J. Manuf. Process. 72 (2021) 294–308, https://doi.org/10.1016/j.jmapro.2021.10.022.

[46] R. Zhou, Y. Liu, B. Liu, J. Li, Q. Fang, Precipitation behavior of selective laser melted FeCoCrNiC0.05 high entropy alloy, Intermetallics. 106 (2019) 20–25, https://doi.org/10.1016/j.intermet.2018.12.001.

[47] W. Wu, R. Zhou, B. Wei, S. Ni, Y. Liu, M. Song, Nanosized precipitates and dislocation networks reinforced C-containing CoCrFeNi high-entropy alloy fabricated by selective laser melting, Mater. Charact. 144 (2018) 605–610, https://doi.org/10.1016/j.matchar.2018.08.019.

[48] R. Zhou, Y. Liu, C. Zhou, S. Li, W. Wu, M. Song, B. Liu, X. Liang, P.K. Liaw, Microstructures and mechanical properties of C-containing FeCoCrNi high-entropy alloy fabricated by selective laser melting, Intermetallics. 94 (2018) 165–171, https://doi.org/10.1016/j.intermet.2018.01.002.

[49] C. Zhang, G.J. Chen, P.Q. Dai, Evolution of the microstructure and properties of laser-clad FeCrNiCoBx high-entropy alloy coatings, Mater. Sci. Technol. (United Kingdom) 32 (2016) 1666–1672, https://doi.org/10.1080/02670836.2015.1138035.

[50] D. Liu, J. Zhao, Y. Li, W. Zhu, L. Lin, Effects of boron content on microstructure and wear properties of FeCoCrNiBx high-entropy alloy coating by laser cladding, Appl. Sci. 10 (2020) 49.

[51] D. Lin, L. Xu, X. Li, H. Jing, G. Qin, H. Pang, F. Minami, A Si-containing FeCoCrNi high-entropy alloy with high strength and ductility synthesized in situ via selective laser melting, Addit. Manuf. 35 (2020), https://doi.org/10.1016/j.addma.2020.101340 101340.

[52] M. Song, R. Zhou, J. Gu, Z. Wang, S. Ni, Y. Liu, Nitrogen induced heterogeneous structures overcome strength-ductility trade-off in an additively manufactured high-entropy alloy, Appl. Mater. Today. 18 (2020) 1–6, https://doi.org/10.1016/j.apmt.2019.100498.

[53] D. Zhao, Q. Yang, D. Wang, M. Yan, P. Wang, M. Jiang, C. Liu, D. Diao, C. Lao, Z. Chen, Z. Liu, Y. Wu, Z. Lu, Ordered nitrogen complexes overcoming strength–ductility trade-off in an additively manufactured high-entropy alloy, Virtual Phys. Prototyp. 15 (2020) 532–542, https://doi.org/10.1080/17452759.2020.1840783.

[54] M. Klimova, D. Shaysultanov, A. Semenyuk, S. Zherebtsov, G. Salishchev, N. Stepanov, Effect of nitrogen on mechanical properties of CoCrFeMnNi high entropy alloy at room and cryogenic temperatures, J. Alloys Compd. 849 (2020), https://doi.org/10.1016/j.jallcom.2020.156633 156633.

[55] J. Zhang, K.N. Yoon, M.S. Kim, H.S. Ahn, J.Y. Kim, W.H. Ryu, E.S. Park, Manipulation of microstructure and mechanical properties in N-doped CoCrFeMnNi high-entropy alloys, Metals (Basel). 11 (2021), https://doi.org/10.3390/met11091487.

[56] J. Zhang, K.N. Yoon, M.S. Kim, H.S. Ahn, J.Y. Kim, Z. Li, T. Sasaki, K. Hono, E.S. Park, Strengthening by customizing microstructural complexity in nitrogen interstitial CoCrFeMnNi high-entropy alloys, J. Alloys Compd. 901 (2022), https://doi.org/10.1016/j.jallcom.2021.163483 163483.

[57] R. Li, P. Niu, T. Yuan, P. Cao, C. Chen, K. Zhou, Selective laser melting of an equiatomic CoCrFeMnNi high-entropy alloy: processability, non-equilibrium microstructure and mechanical property, J. Alloys Compd. 746 (2018) 125–134, https://doi.org/10.1016/j.jallcom.2018.02.298.

[58] C. Zhang, K. Feng, H. Kokawa, B. Han, Z. Li, Cracking mechanism and mechanical properties of selective laser melted CoCrFeMnNi high entropy alloy using different scanning strategies, Mater. Sci. Eng. A. 789 (2020), https://doi.org/10.1016/j.msea.2020.139672 139672.

[59] B.H. Toby, CMPR – a powder diffraction toolkit, J. Appl. Crystallogr. 38 (2005) 1040–1041, https://doi.org/10.1107/s0021889805030232.

[60] H.Y. Wan, Z.J. Zhou, C.P. Li, G.F. Chen, G.P. Zhang, Effect of scanning strategy on grain structure and crystallographic texture of Inconel 718 processed by selective laser melting, J. Mater. Sci. Technol. 34 (2018) 1799–1804, https://doi.org/10.1016/j.jmst.2018.02.002.

[61] L. Liu, Q. Ding, Y. Zhong, J. Zou, J. Wu, Y.L. Chiu, J. Li, Z. Zhang, Q. Yu, Z. Shen, Dislocation network in additive manufactured steel breaks strength–ductility trade-off, Mater. Today. 21 (2018) 354–361, https://doi.org/10.1016/j.mattod.2017.11.004.

[62] C. Kenel, N.P.M. Casati, D.C. Dunand, 3D ink-extrusion additive manufacturing of CoCrFeNi high-entropy alloy micro-lattices, Nat. Commun. 10 (2019) 1–8, https://doi.org/10.1038/s41467-019-08763-4.

[63] D. Lin, L. Xu, Y. Han, Y. Zhang, H. Jing, L. Zhao, F. Minami, Structure and mechanical properties of a FeCoCrNi high-entropy alloy fabricated via selective laser melting, Intermetallics. 127 (2020), https://doi.org/10.1016/j.intermet.2020.106963 106963.

[64] Y. Kuzminova, D. Firsov, A. Dudin, S. Sergeev, A. Zhilyaev, A. Dyakov, A. Chupeeva, A. Alekseev, D. Martynov, I. Akhatov, S. Evlashin, The effect of the parameters of the powder bed fusion process on the microstructure and mechanical properties of CrFeCoNi medium-entropy alloys, Intermetallics. 116 (2020), https://doi.org/10.1016/j.intermet.2019.106651 106651.

[65] Z.G. Zhu, Q.B. Nguyen, F.L. Ng, X.H. An, X.Z. Liao, P.K. Liaw, S.M.L. Nai, J. Wei, Hierarchical microstructure and strengthening mechanisms of a CoCrFeNiMn high entropy alloy additively manufactured by selective laser melting, Scr. Mater. 154 (2018) 20–24, https://doi.org/10.1016/j.scriptamat.2018.05.015.

[66] L. Guo, J. Gu, B. Gan, S. Ni, Z. Bi, Z. Wang, M. Song, Effects of elemental segregation and scanning strategy on the mechanical properties and hot cracking of a selective laser melted FeCoCrNiMn-(N, Si) high entropy alloy, J. Alloys Compd. 865 (2021), https://doi.org/10.1016/j.jallcom.2021.158892.

[67] X. Wang, X. Pan, P. Sun, C. Qiu, Significant enhancement in tensile strength and work hardening rate in CoCrFeMnNi by adding TiAl particles via selective laser melting, Mater. Sci. Eng. A 831 (2022), https://doi.org/10.1016/j.msea.2021.142285 142285.

[68] B. Li, L. Zhang, Y. Xu, Z. Liu, B. Qian, F. Xuan, Selective laser melting of CoCrFeNiMn high entropy alloy powder modified with nano-TiN particles for additive manufacturing and strength enhancement: Process, particle behavior and effects, Powder Technol. 360 (2020) 509–521, https://doi.org/10.1016/j.powtec.2019.10.068.

[69] Y.T. Lin, X. An, Z. Zhu, M.L.S. Nai, C.W. Tsai, H.W. Yen, Effect of cell wall on hydrogen response in CoCrFeMnNi high-entropy alloy additively manufactured by selective laser melting, J. Alloys Compd. 925 (2022), https://doi.org/10.1016/j.jallcom.2022.166735 166735.

[70] M. Shih, J. Miao, M. Mills, M. Ghazisaeidi, Stacking fault energy in concentrated alloys, Nat. Commun. 12 (2021) 1–10, https://doi.org/10.1038/s41467-021-23860-z.

[71] R.P. Reed, R.E. Schramm, Relationship between stacking-fault energy and x-ray measurements of stacking-fault probability and microstrain, J. Appl. Phys. 45 (1974) 4705–4711, https://doi.org/10.1063/1.1663122.

[72] B.E. Warren, X-ray Diffraction, Courier Corporation (1990).

[73] P.H. Adler, G.B. Olson, W.S. Owen, Strain hardening of hadfield manganese steel, Metall. Mater. Trans. A. 17 (1986) 1725–1737, https://doi.org/10.1007/BF02817271.

[74] A.W. Sleeswykt, Ductile cleavage fracture, yielding and twinning in a-iron, Acta Metall. 11 (1963) 187–194.

[75] M. Schneider, G. Laplanche, Effects of temperature on mechanical properties and deformation mechanisms of the equiatomic CrFeNi medium-entropy alloy, Acta Mater. 204 (2021), https://doi.org/10.1016/j.actamat.2020.11.012 116470.

[76] Z. Wu, H. Bei, G.M. Pharr, E.P. George, Temperature dependence of the mechanical properties of equiatomic solid solution alloys with face-centered cubic crystal structures, Acta Mater. 81 (2014) 428–441, https://doi.org/10.1016/j.actamat.2014.08.026.

[77] M. Lugovy, V. Slyunyayev, M. Brodnikovskyy, Solid solution strengthening in multicomponent fcc and bcc alloys: Analytical approach, Prog. Nat. Sci. Mater. Int. 31 (2021) 95–104, https://doi.org/10.1016/j.pnsc.2020.11.006.

[78] H.G. Li, Y.J. Huang, W.J. Zhao, T. Chen, J.F. Sun, D.Q. Wei, Q. Du, Y.C. Zou, Y.Z. Lu, P. Zhu, X. Lu, A.H.W. Ngan, Overcoming the strength-ductility trade-off in an additively manufactured CoCrFeMnNi high entropy alloy via deep cryogenic treatment, Addit. Manuf. 50 (2022) 1–12, https://doi.org/10.1016/j.addma.2021.102546.

[79] H.A. Roth, C.L. Davis, R.C. Thomson, Modeling solid solution strengthening in nickel alloys, Metall. Mater. Trans. A Phys. Metall. Mater. Sci. 28 (1997) 1329–1335, https://doi.org/10.1007/s11661-997-0268-2.

[80] G.I. Taylor, Plastic strain in metals, J. Inst. Met. 62 (1938) 307–324.

[81] G. Vastola, Q.X. Pei, Y.W. Zhang, Predictive model for porosity in powder-bed fusion additive manufacturing at high beam energy regime, Addit. Manuf. 22 (2018) 817–822, https://doi.org/10.1016/j.addma.2018.05.042.

[82] M. Naeem, H. He, S. Harjo, T. Kawasaki, W. Lin, J.J. Kai, Z. Wu, S. Lan, X.L. Wang, Temperature-dependent hardening contributions in CrFeCoNi high-entropy alloy, Acta Mater. 221 (2021), https://doi.org/10.1016/j.actamat.2021.117371 117371.

[83] Y. Chen, Q. Zhao, H. Wu, Q. Fang, J. Li, Effect of interstitial N atom on physical and mechanical properties of FeCoCrNiMn high-entropy alloys: a first-principles study, Phys. B Condens. Matter. 615 (2021), https://doi.org/10.1016/j.physb.2021.413078 413078.

[84] G.K. Williamson, R.E. Smallman III, Dislocation densities in some annealed and cold-worked metals from measurements on the X-ray Debye-Scherrer spectrum, Philos. Mag. 1 (1956) 34–46, https://doi.org/10.1080/14786435608238074.

[85] T. Pandiyarajan, B. Karthikeyan, Cr doping induced structural, phonon and excitonic properties of ZnO nanoparticles, J. Nanopart. Res. 14 (2012), https://doi.org/10.1007/s11051-011-0647-x.

[86] S. Curtze, V.T. Kuokkala, Dependence of tensile deformation behavior of TWIP steels on stacking fault energy, temperature and strain rate, Acta Mater. 58 (2010) 5129–5141, https://doi.org/10.1016/j.actamat.2010.05.049.

[87] W.S. Owen, M. Grujicic, Strain aging of austenitic hadfield manganese steel, Acta Mater. 47 (1998) 111–126, https://doi.org/10.1016/S1359-6454(98)00347-4.

[88] D. Barbier, N. Gey, S. Allain, N. Bozzolo, M. Humbert, Analysis of the tensile behavior of a TWIP steel based on the texture and microstructure evolutions, Mater. Sci. Eng. A. 500 (2009) 196–206, https://doi.org/10.1016/j.msea.2008.09.031.

[89] C. Efstathiou, H. Sehitoglu, Strain hardening and heterogeneous deformation during twinning in Hadfield steel, Acta Mater. 58 (2010) 1479–1488, https://doi.org/10.1016/j.actamat.2009.10.054.

[90] M. Lindroos, A. Laukkanen, G. Cailletaud, V.T. Kuokkala, On the effect of deformation twinning and microstructure to strain hardening of high manganese austenitic steel 3D microstructure aggregates at large strains, Int. J. Solids Struct. 125 (2017) 68–76, https://doi.org/10.1016/j.ijsolstr.2017.07.015.

[91] F. Shen, J. Zhou, Y. Liu, R. Zhu, S. Zhang, Y. Wang, Deformation twinning mechanism and its effects on the mechanical behaviors of ultrafine grained and nanocrystalline copper, Comput. Mater. Sci. 49 (2010) 226–235, https://doi.org/10.1016/j.commatsci.2010.04.044.